ADVANCED MATERIALS
www.advmat.de

Fabrication of Arrays of Topological Solitons in Patterned Chiral Liquid Crystals for Real-Time Observation of Morphogenesis

Geonhyeong Park, Ahram Suh, Hanqing Zhao, Changjae Lee, Yun-Seok Choi, Ivan I. Smalyukh, and Dong Ki Yoon**

Topological solitons have knotted continuous field configurations embedded in a uniform background, and occur in cosmology, biology, and electromagnetism. However, real-time observation of their morphogenesis and dynamics is still challenging because their size and timescale are enormously large or tiny. Liquid crystal (LC) structures are promising candidates for a model-system to study the morphogenesis of topological solitons, enabling direct visualization due to the proper size and timescale. Here, a new way is found to rationalize the real-time observation of the generation and transformation of topological solitons using cholesteric LCs confined in patterned substrates. The experimental demonstration shows the topologically protected structures arise via the transformation of topological defects. Numerical modeling based on minimization of free energy closely reconstructs the experimental findings. The fundamental insights obtained from the direct observations pose new theoretical challenges in understanding the morphogenesis of different types of topological solitons within a broad range of scales.

1. Introduction

Topological solitons have been found in many branches of science, ranging from atomic physics to condensed matter and cosmology,[1–8] which are localized continuous field configurations that cannot be smoothly transformed to a uniform state.[9] They are stabilized with chiral or nonlinear free energy terms,[10,11] which are required to overcome the stability constraints imposed by the Derrick theorem.[12] Recently, significant interest arises in investigating topological solitons with condensed matters, especially the cholesteric (Ch) liquid crystal (LC).[13–29] It can be rationalized due to the ease of controlling and observing LC structures in virtue of the anisotropic feature of the LC phase, which is originated from the long-range ordered molecular director (**n**), where **n** is a headless unit vector representing the average orientation of the local LC molecules.[30] This is why one can directly observe the topological solitons in the Ch phase, enabling the use of LC topological solitons as model systems for classical field theory[2–5,18–20,29] or applied to various optical systems.[16,17,25] Usually, the LC topological solitons are created using laser tweezers,[13–15,17–22,25,27,29] topographic confinement,[23,26] and external fields.[15,16,24,28] However, the detailed kinetics and transformation of topological solitons in the previous studies are hard to observe because they were randomly formed or relaxed to equilibrium within a short time.[13–29]

G. Park, C. Lee, Y.-S. Choi, D. K. Yoon
Department of Chemistry
Korea Advanced Institute of Science and Technology (KAIST)
Daejeon 34141, Republic of Korea
E-mail: nandk@kaist.ac.kr

A. Suh, D. K. Yoon
Graduate School of Nanoscience and Technology
Korea Advanced Institute of Science and Technology
Daejeon 34141, Republic of Korea

H. Zhao, I. I. Smalyukh
Department of Physics and Soft Materials Research Center
University of Colorado
Boulder, CO 80309, USA
E-mail: Ivan.Smalyukh@colorado.edu

I. I. Smalyukh
Materials Science and Engineering Program
University of Colorado
Boulder, CO 80309, USA

I. I. Smalyukh
Renewable and Sustainable Energy Institute
National Renewable Energy Laboratory and University of Colorado
Boulder, CO 80309, USA

D. K. Yoon
KAIST Institute for Nanocentury
Korea Advanced Institute of Science and Technology (KAIST)
Daejeon 34141, Republic of Korea

The ORCID identification number(s) for the author(s) of this article can be found under https://doi.org/10.1002/adma.202201749.

DOI: 10.1002/adma.202201749

Here, we experimentally demonstrate that the periodic air pockets within the Ch LC medium lead to the well-ordered topological defects that can be reliably transformed to topological solitons, which have proper time and size scales to observe the morphogenesis by polarized optical microscopy (POM).[31,32] In addition to the experimental approach, we reconstruct the 3D **n**-field configurations by minimizing Landau–de Gennes free energy based on the Q-tensor approach and discuss how the topological solitons relate to the given boundary conditions.[33–35] The proposed platform can be fabricated facilely than the current topological soliton array fabrication processes and is expected to provide a new perspective to analyze various topological solitons.

2. Results and Discussions

A sandwiched cell is prepared with the periodic micropatterned silicon wafer and cover glass. Both substrates are coated with vertical alignment polyimide to induce strong perpendicular anchoring conditions (≈10^{-4} J m^{-2}).[36] The micropatterns have cylindrical holes, where the diameter is 20 µm, and the depth is 5 µm, which are arranged with a square lattice with various spacing (*sp*) (**Figure 1**a). The Ch LC is prepared by mixing 4-cyano-4″-pentylbiphenyl (5CB) and chiral dopant (S)-4-cyano-4″-(2-methyl butyl) biphenyl (CB15), which has the helical pitch (*p*) ≈ 7 µm at 30 °C (Figure S1, Supporting Information).

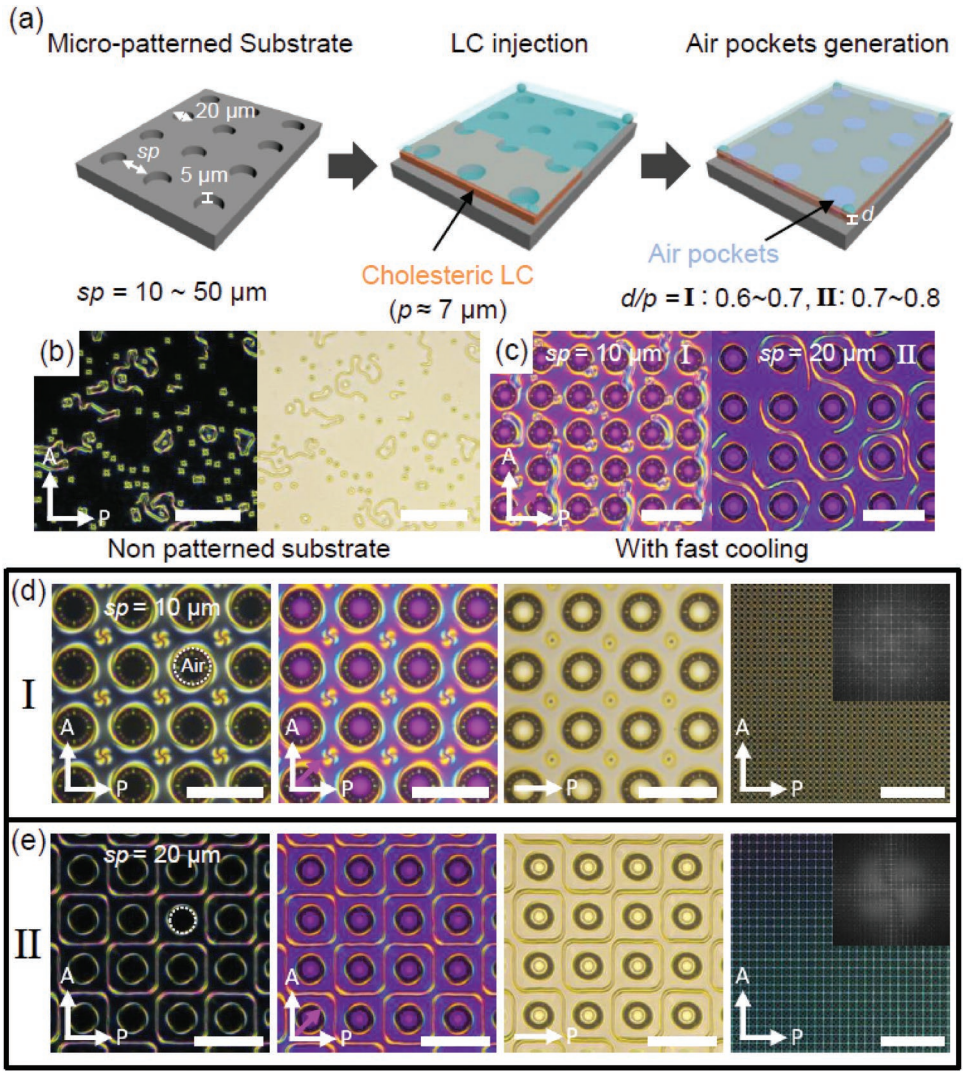

Figure 1. Patterned substrates and enabled highly ordered solitonic structures. a) Schematic illustrations of micropatterned silicon substrates. The sandwich cell is made of the glass substrate and the patterned substrate, where both substrates are treated with vertical alignment polyimide. The cell gap (*d*) is controlled to ≈4.2–4.9 µm (I) and ≈4.9–5.6 µm (II). b) Experimental images of randomly arranged solitonic structures for the nonpatterned substrates. From the left, the images are obtained with a POM and optical microscopy images. c) Experimental POM images with a phase retardation plate (λ = 530 nm) obtained for samples with patterned substrates when the Ch LCs are fast cooled at −2 °C min^{-1} rate. d,e) Experimental images of highly ordered torons (d) and cholesteric (e) fingers. From the left, POM, POM with a retardation plate, optical microscopy images with a polarizer, and large-area POM images, respectively. In the large-area images, the insets are the corresponding Fourier transformed images. The white or black arrows indicate the direction of the polarizers, and the magenta arrows indicate the slow axis of the retardation plate. Scale bars: 50 µm (b,c,e), 40 µm (d), but in the rightmost images in d,e), it is 300 µm.

The confinement ratio of the cells (d/p) is controlled from ≈0.5 to 1.1, where d is the cell gap. The Ch LC is injected into the sandwich cell at the isotropic (Iso) temperature, 40 °C, by a capillary force. Due to the different capillary actions, the LC materials cannot fill inside the patterned area and thus spontaneously generate the regularly arranged air pockets, which leads to generating specific topological defects[31,37,38] by confining the LC with strong perpendicular anchoring conditions. After injection, the cell slowly cools down to the Ch temperature, 30 °C, with −0.25 °C min^{-1} cooling rates. Samples under the topographic confinement exhibit highly ordered birefringent textures with air pockets on cooling (Figure 1d,e), which are quite different from optical textures formed without topographic patterns (Figure 1b) or with a rapid cooling condition (Figure 1c). The confinement ratio ranges from d/p = ≈0.6–0.7 (case I) for pinwheel-shaped structures in Figure 1d to d/p = ≈0.7–0.8 (case II) for line-shaped textures in Figure 1e. Low magnified images with the corresponding Fourier transform patterns (rightmost images in Figure 1d,e) confirm that the formation of these structures is very uniform over several mm^2 under our experimental conditions. In case I, the pinwheel-shaped structures are torons, where 2D topological solitons called skyrmions are embedded in 3D space between two plates with strong perpendicular anchoring.[13–23] Their localized **n**-field configurations twist along all spatial dimensions, which are stabilized in the topologically trivial boundary conditions by strong energy barriers accompanied with the generation of topological defects near the substrates. In case II, the interconnected line textures are cholesteric fingers of the third kind (CF-3s), in which 1D topological solitons called twist walls are embedded in 3D space.[21–24] CF-3s are composed of **n**-fields π-twisted along one axis, which is stabilized by two twist disclination lines near the top and bottom substrates.

The morphogenesis of the arrayed torons is directly investigated by POM with the phase retardation plate (**Figure 2**; and Movie S1, Supporting Information). The thermal capacity is about three times lower for the air pocket than for LC,[39] inducing the temperature gradient among the air pockets (Figure S2, Supporting Information), enabling real-time observation of the transformation of the solitonic structures on cooling. Nucleation of the Ch phase occurs from the air-LC interface (Figure 2a,b).[31–32] When the Ch LC domains merge on further cooling, birefringent textures wholly occupy the sample, except the air pockets (Figure 2c,d). Here, one disclination loop, denoted as defect-1 (marked red dashed square in Figure 2d–g; and Figure S3, Supporting Information), is generated by pinning their edges at the adjacent four air pockets. Then another disclination loop, denoted as defect-2 (marked the dark blue in Figure 2e–g; and Figure S3, Supporting Information), emerges in defect-1. On further cooling, magenta color domains appear again around defect-1, where the Ch LC becomes the uniformly unwound state as the temperature decreases (Figure 2f–h). The Ch LC domains containing defect-1 and defect-2 gradually shrink into localized structures within a uniform background (Figure 2g,h; and Movie S1, Supporting Information). The topological solitons are regularly created in the final stage, exhibiting a clockwise rotating pinwheel texture that does not disappear or break (Figure 2h).

The **n**-field configurations are reconstructed by minimizing the free energy (details in the Experimental Section) for the same conditions as in experiments.[33–35] The simulated results are in good agreement with the experiments images (Figure 2i,j; and Figure S4, Supporting Information), with the scalar order parameter defined as $S = \left\langle \left(\frac{3\cos^2\theta - 1}{2} \right) / 2 \right\rangle$, where θ is the angle between the molecular axis and the local director (Figure 2k,l).[30] The comparison of experimental and computer-simulated results demonstrates that the localized structures are T3-2 type of torons, where a point defect and a disclination loop confine the 2D skyrmion.[13] In addition, two cross-sections of $\mathbf{n}_z$ (Figure 2m) and its 3D isosurfaces (Figure 2n) show the 3D **n**-field configurations of T3-2s and topological defects arrangement, where the point defect and disclination ring defect appear near the top and bottom substrates, respectively. As shown in Figure 2a, the inner and outer circles of the air pockets are distinguished, indicating that the air pockets are not cylinders but conical frustums with a smaller diameter on the top (Figure S5, Supporting Information). The change of diameter of the air pockets along the z-axis can stabilize different topological defects with the same charge near the substrates, analogously to the appearance of hedgehog and Saturn ring defects in the nematic colloids according to the cell thickness.[40] We obtain insights into how T3-2s are stabilized at specific locations from the changes of optical textures, despite the complex transformation of T3-2s. Defect-1s and defect-2s are sequentially generated by the complementary contribution of the air pockets and the substrate, which act as seeds for T3-2s. At the early stage, the textures surrounding defect-2s show counter-clockwise features (Figure 2e–g), while the final T3-2 textures show clockwise features. The observed direction of rotation is determined by how the LCs are mainly arranged in the in-plane direction. In general, T3-2 has opposite spiraling in-plane **n**-field configurations at the upper and lower defect planes.[13] Therefore, the direction of the pinwheel-shaped texture observed through the POM is determined according to which side of the cell contributes to the observed image. Based on this consideration, it is possible to qualitatively uncover the sequential transformation of the topological defects during the phase transition. Defect-1 and defect-2 created in the form of disclination rings in the initial stage (Figure 2e) shrink as the temperature decreases. At the intermediate stage, when defect-1 has a larger radius than defect-2, a complex texture is observed where a clockwise rotating pinwheel wraps around a counter-clockwise rotating pinwheel (Figure S6, Supporting Information). Simulation results show that this texture can be observed when one large ring defect (defect-1) is on top, and a small ring defect (defect-2) is underneath. When the defect-1 is large enough, clockwise rotating **n**-field configurations near the lower defect plane can be observed by POM because the LCs located inside the defect-1 are aligned perpendicular to the substrate. During the contraction, the small pinwheel disappears, and it is observed that the rotation direction of the entire texture is reversed. This occurs roughly when the radius of the defect ring at the top becomes smaller than that at the bottom. In detail, the little pinwheel seems to disappear here because the **n**-field at the top is no longer perpendicular to the substrate, but changes to adefect, and the signal passing through

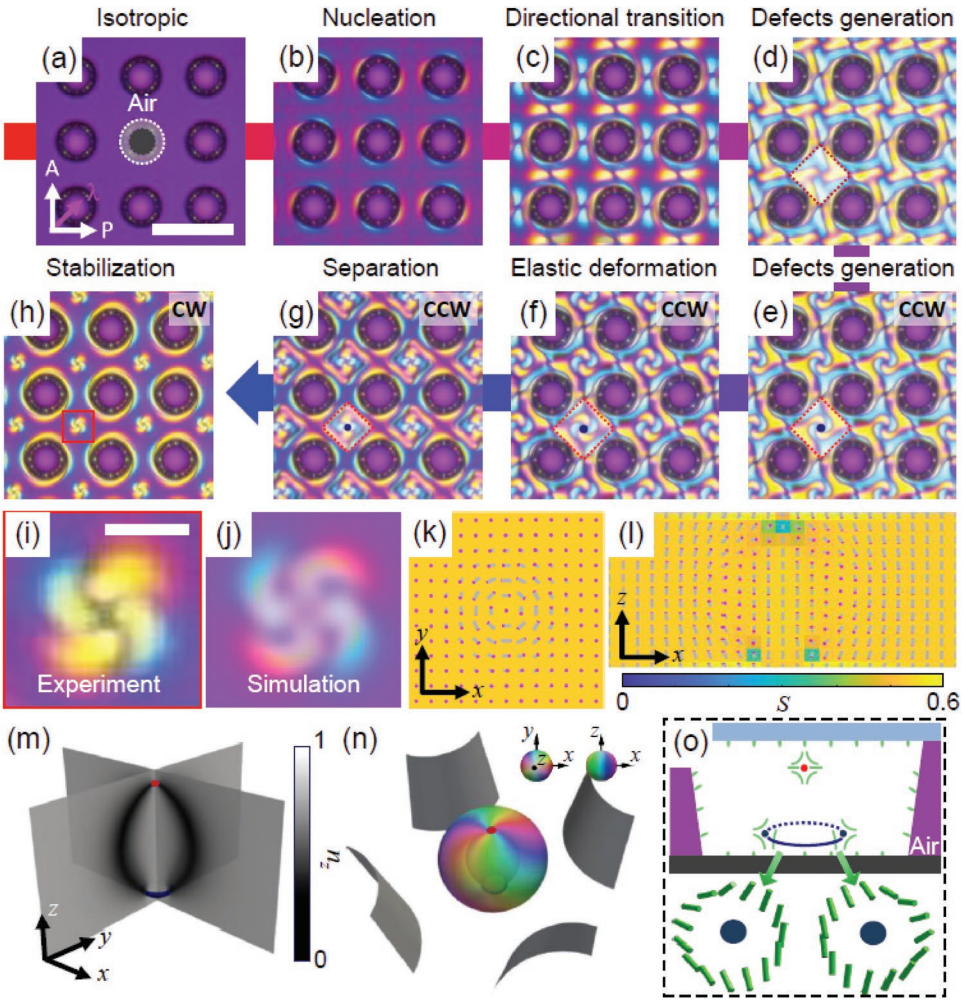

Figure 2. Nucleation of torons from topological defects. a–h) Experimental images of sequential phase transition of the toron cooled with –0.25 °C min^{-1} and obtained by POM with a retardation plate. The white and gray circles in (a) indicate the lateral extent of the frustum-shaped air pockets. b) Birefringent regions nucleate at the air pockets. c) Kinetically directional phase transition occurs due to the difference in heat capacity. d,e) Defect-1s (red dashed line) and defect-2s (dark blue circle) are generated. f) After elastic deformation toward energy-minimized **n**-field configurations, g) LCs outside the defect-1s rearrange to the uniformly unwound state. h) The pinwheel-shaped domains shrink and stabilize into the highly ordered T3-2s. i,j) High-magnification experimental (i) and simulated (j) POM images of the T3-2. k,l) Scalar order parameter patterns and computer-simulated **n**-field for the T3-2s at the *xy*-midplane (k) and *xz*-plane (l) cross-sections. m) 3D view of $\mathbf{n}_z$ and topological defects in the *xz*- and *yz*-midplane cross-sections. n) Isosurface depicts the **n**-field configurations of T3-2 at $n\mathbf{n}_z = 0.577$. The coloring of the isosurface depends on azimuthal and polar angles, as the insets show. The gray surfaces indicate air pockets. o) Schematic illustration of **n** configurations (green cylinders) at the surfaces and topological defects. In (m–o), point defects and disclination loops are shown in red and dark blue, with **n** surrounding the disclination loop shown in the bottom insects. Numerical results are obtained for 5CB material parameters at $d/p = 0.6$. Scale bars: 40 µm (a–h) and 5 µm (i).

this region overlaps the signal from the **n**-field in the bottom defect ring (Figure 2g,h; and Figure S6 and Movie S1, Supporting Information). At the final stage, defect-1 contracts as a point defect near the top substrate, and defect-2 become stabilized as a disinclination ring defect near the bottom substrate under the influence of different geometry and anchoring conditions originating from the shape of the air pockets (Figure S5, Supporting Information). Periodically arranged T3-2s are not observed where topological defects cannot be controlled in the intermediate stage (Figure 1b,c). These experimental findings demonstrate that topological solitons can be created as designed if topological defects can be managed proactively during phase transitions, as in previous simulation studies using artificial defects to reconstruct solitonic structures.[13,15,21,23]

The morphogenesis of the CF-3s loop is directly investigated by POM (**Figure 3**; and Movie S2, Supporting Information). In the early stages of the phase transition from the Iso to Ch phase, the Ch LC domain is nucleated at the air pockets, which is similar to Figures 2 and 3a,b). After further cooling, the ring-shaped domains appear, resulting from the merging of nematic domains with degenerated surface anchoring conditions of the Iso-Ch interface (Figure 3c,k). When the neighboring ring-shaped domains extending from the air pockets are combined, linear structures of a square grid are formed (Figure 3d,i,j). At this time, disclination line defects are generated near the

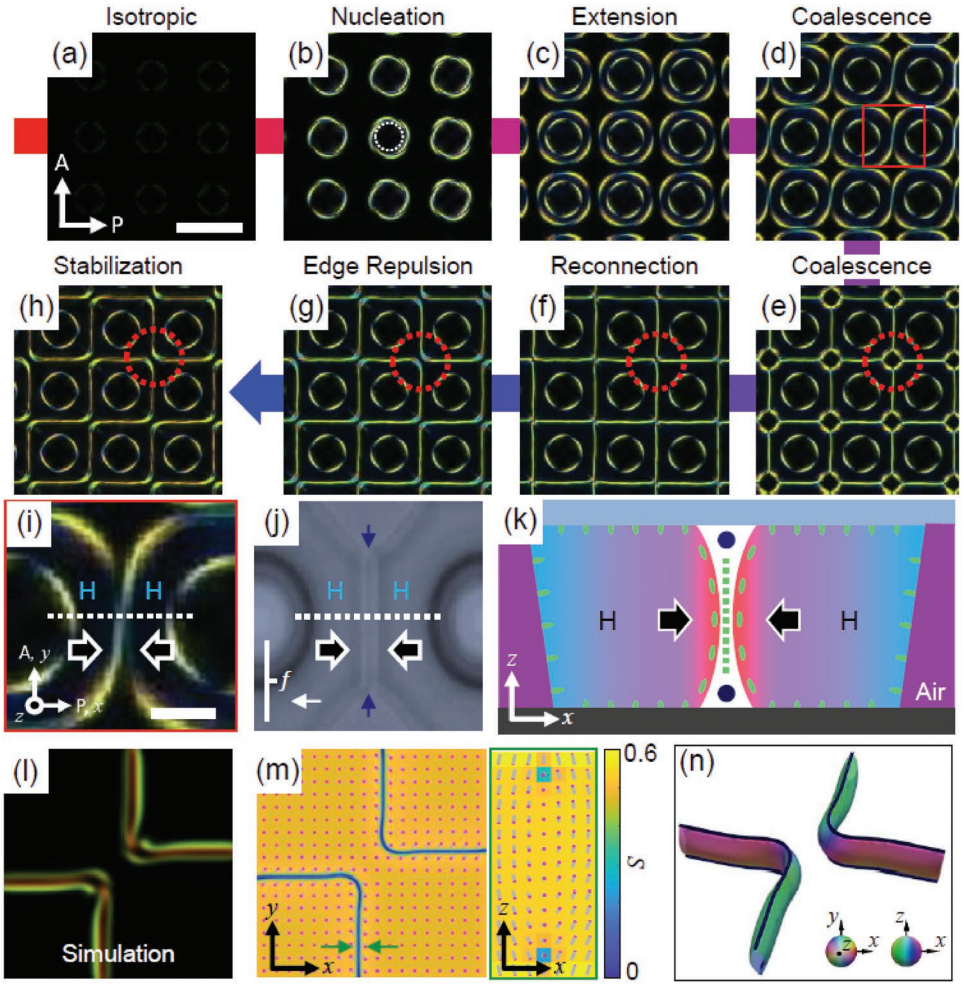

Figure 3. Transformation of cholesteric fingers mediated by topological defects. a–h) Experimental images of sequential phase transition of the CFs cooled with –0.25 °C min^{-1} and obtained with POM. b,c) LCs nucleate and form ring-shaped domains at the air interfaces. d,e) The extending domains merge to form line structures. e–h) As shown in red dashed circles, the line structures are connected, form closed loops, and rearrange their positions. After stabilization, CF-3 loops are stabilized along the square lattice. i,j) A magnification POM image and an out-of-focus optical microscopy image with monochrome ($\lambda = 525$ nm) at red box in (d). The area marked with "H" is the LCs perpendicularly aligned to the substrates. k) Schematic illustration of **n**-field configurations in the *xz*-plane cross-section at the region marked by white dashed lines at (i,j). l) The simulation POM image of CF-3s. m) Scalar order parameter patterns and computer-simulated **n**-field configurations for the CF-3s at the *xy*-plane cross-section located at the bottom defect plane (left) and *xz*-plane cross-sections marked by green arrows (right). n) Isosurface depicts the **n**-field configurations of CF-3s at $\mathbf{n}_z = 0.577$. The coloring of isosurface depends on the azimuthal and polar angle, as the insets show. The line defects are marked by dark blue arrows in (j) and circles in (k). Numerical results are obtained for 5CB material parameters at $d/p = 0.7$. Scale bars: 40 µm (a–h) and 10 µm (i).

substrates, as shown in a schematic illustration of the coalescence of adjacent interfaces (Figure 3k) and an out-of-focus optical microscopy image (Figure 3j). The line structures reconnect to form closed loops of the square grid as the isotropic regions disappear in the whole area (Figure 3e–g). In the final stages, the line structures at the corners of the square grid repel each other to be stabilized while maximizing the spacing between them (Figure 3g,h). The resultant line structure is expected to be CF-3, within which a 1D topological soliton (twist wall) is terminated on two twist disclination lines near the top and bottom confining substrates.[17,21–24] To make this clear, **n**-field configurations of CF-3s are reconstructed with the same method as used in Figure 2 (detailed in the Experimental Section). As shown in Figure 3l, the computer-simulated POM image matches the experimental results. In **n**-field configurations with scalar order parameter patterns in the *xy*- and *xz*-cross-sections, two disclination line defects are located near the substrates, and the π-twisted **n**-field configurations along the *x*-axis are embedded within these two line defects (Figure 3m). In addition, the isosurface of CF-3s provides that a 3D view of the 1D topological soliton is capped between two twist disclinations (Figure 3n). During the phase transition, the generation of the line defects stabilizes the closed CF-3 loop configurations (Figure 3i–k). These lines are connected and form disclination loops without unstable ends (Figure S7i–l, Supporting Information). At the same time, the disclination loops allow the twisted **n**-field configurations to be accommodated along with the loops within a uniform background without breakage at given boundary conditions. Highly arranged CF-3s loops are not observed when disclination loops cannot be controlled

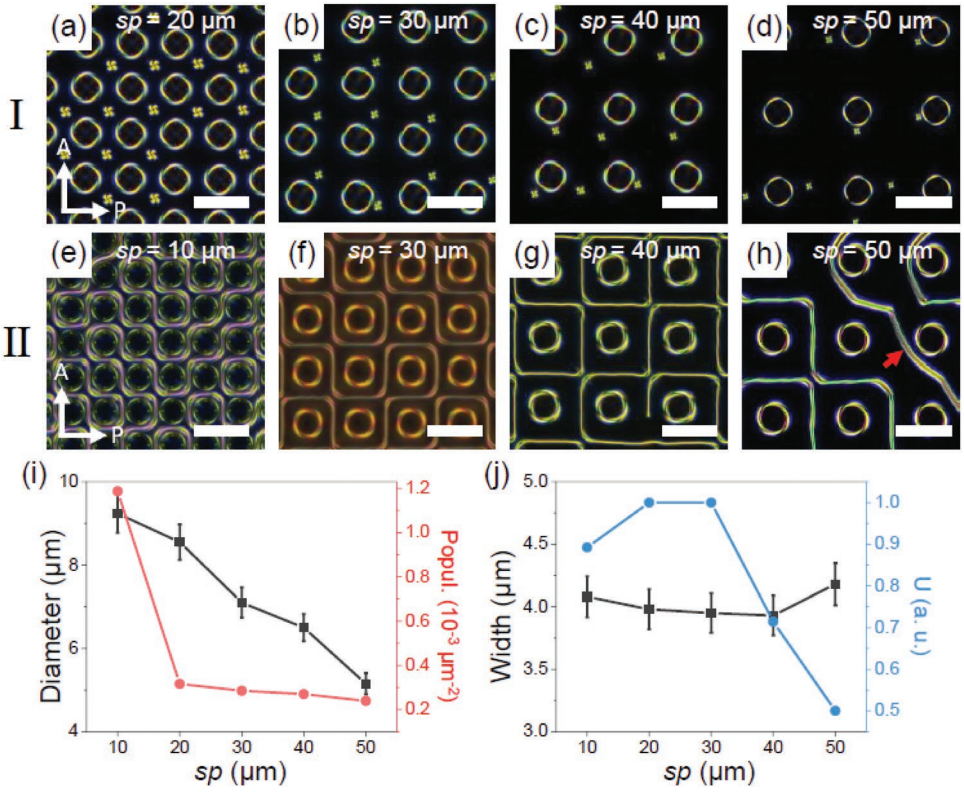

Figure 4. POM images of torons and CFs for various lattice spacings. a–d) Experimental POM images of the torons when *sp* = 20 μm (a), 30 μm (b), 40 μm (c), and 50 μm (d). As *sp* increases, the size, density, and uniformity of the torons decrease. e–h) Experimental POM images of the CFs when *sp* = 10 μm (e), 30 μm (f), 40 μm (g), and 50 μm (h). As *sp* increases, the widths and the uniformity of the CF-3s decrease. The red arrow in (h) indicates a cholesteric finger of wider widths. i) Average diameter (black) and number density (red) of torons, and j) average width and uniformity of CFs. The toron diameter and CF width data are obtained by measuring 30 objects. The error bars represent ± one standard deviation. Scale bars: 50 μm.

during the phase transition (Figure 1b,c). In these cases, disclinations are randomly generated due to unmanaged generation sites, resulting in fragmented CF-3s rather than closed loops. Eventually, most of the fragmented CF-3s disappear because of their unstable ends. These findings demonstrate that if the line disclination can be controlled as desired, 1D topological solitons can be embedded into 3D space as intended complex geometric configurations with the help of these disclinations.

The air pocket plays two important roles: providing a directional thermal gradient during the Iso-Ch phase transition and defining the perpendicular anchoring condition. To investigate the effect of air pocket on the arrangement of solitonic structures, *sp* is varied from 10 to 50 μm for cases I and II. At *sp* = 20 μm in case I, an incomplete array of torons is observed (**Figure 4**a). The only difference compared to torons in Figure 2 is that the room between air pockets is too large to maintain a uniform directional thermal gradient. The effect of thermal gradient between the air pockets gradually decreases as *sp* increases (Figure S8, Supporting Information). Instead of forming a periodic topological defects array, ring-shaped domains appear. Some of them are geometrically constrained by adjacent air pockets and transform into torons. This process occurs randomly by uneven cooling within larger volumes, resulting in an irregular toron arrangement (Figure S9a, Supporting Information). At *sp* = 30 μm, the uniformity of T3-2s arrays deteriorates because the space for stabilization becomes larger (Figure 4b). When *sp* further increases up to ≈40–50 μm, the regular temperature gradients created by air pockets no longer occur, and nucleation of the Ch LCs happens all over the area regardless of the air pockets positions (Figure S9b and Movie S4, Supporting Information). As a result, a randomly arranged torons array is observed (Figure 4c,d). As *sp* increases, the average diameter of the torons decreases from ≈9 to ≈5 μm (Figure 4i), and the number of torons per unit area decreases because the contribution of the perpendicular anchoring of the air pockets becomes weaker (Figure 4j). In addition, when the air pockets become further apart, the distance between the torons increases, and their distribution becomes more random (Figure S10, Supporting Information).

CF-3s generated at relatively larger d/p than torons show a similar phase transition behavior over the entire *sp* ranging from 10 to 50 μm (Figure 4e–h; and Figure S9c,d and Movies S2, S5, and S6, Supporting Information). The average width of CFs decreases by about 4% as *sp* increases from 10 to 40 μm, which comes from the weakened contribution of the air pockets such as perpendicular anchoring and geometrical confinement. This trend is also well-reconstructed in the computer-simulated results. (Figure S11, Supporting Information). However, the average width slightly increases at *sp* = 50 μm, which might result from wider CF-1 and CF-2 indicated by red arrows in

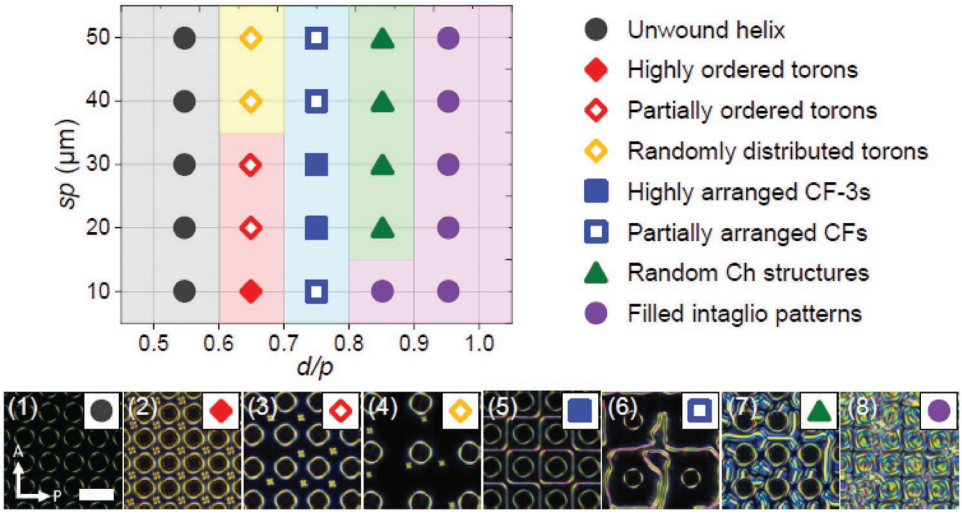

Figure 5. Eight distinct types of Ch structures versus d/p and sp between air pockets. In the diagram, the eight types of different structures are marked by colored segments for a given set of (sp, d/p) conditions. The corresponding experimental POM textures illustrate these eight types: 1) unwound helices due to the low d/p; 2) highly ordered torons from the transformation of predetermined topological defects during the phase transition; 3) partially ordered torons due to the contribution of thermal fluctuation; 4) randomly distributed torons due to larger rooms between air pockets; 5) highly arranged CF-3s due to the precisely controlled the line disclination defects during the phase transition; 6) partially arranged CFs due to disturbed the generation of topological defects; 7) random Ch structures due to the high d/p; 8) the difference of capillary forces become almost identical due to the large d. As a result, the LCs are even filled in the intaglio patterns. Scale bars: 40 μm.

Figure 4h.[24] They are composed of 2π-twisted **n**-field configurations, expected to be occasionally developed from the uneven nucleation of the Ch LC domains (Figure S9d and Movie S6, Supporting Information). Besides, as sp increases, it is observed that the CF-3s deviate from the straight line or the square grids. The uniformity of CF-3s is quantitively defined as follows: Uniformity = 1 – (the number of unit lattices including dislocation/the number of total unit lattices). Connected CF-3 loops forming perfect square grids are observed at $sp \approx$ 20–30 μm (Uniformity = 1). At sp = 10 μm, it is found that some CF-3s deviate from the straight lines because the contribution of the air pockets is excessive due to the narrow space (Uniformity = 0.89). For sp = ≈40–50 μm, nucleation occurs everywhere in the sample, generating different CFs or disrupting the formation of CF-3 lattices. Therefore, the uniformity becomes low (Uniformity ≈ 0.5–0.72).

To demonstrate all possible structures and arrangements of topological solitons in our platform, the experiments are performed in the entire $d/pd/p$ range between 0.4 and 1.1 with 0.1 increments for different sp ranging from 10 to 50 μm. The experiments are performed more than ten times for each condition, showing high repeatability. The resultant behavior is summarized in the diagram (**Figure 5**), showing eight different types of the Ch LC structures:

1) Distinct birefringent textures are not observed except near the air pockets in all sp ranges because the helix of the Ch LCs is unwound due to the small d/p (Figure S12a and Movie S7, Supporting Information);
2) Highly ordered T3-2s array is transformed from predetermined topological defects at sp = 10 μm (Figures 1d and 2; and Movie S1, Supporting Information);
3) As sp increases, the uniformity of the torons array deteriorates because distances between the air pockets become larger, resulting in uneven cooling (Figure 4a,b; and Figure S9a and Movie S3, Supporting Information);
4) The distribution of torons is randomized because nucleation occurs everywhere in the sample. (Figure 4c,d; and Figure S9b and Movie S4, Supporting Information);
5) Closed CF-3 loops forming square grids are generated through the precisely controlled disclination line defects (Figures 1e and 3; and Movie S2, Supporting Information);
6) Relatively lower uniformity of CF-3 loops is observed because uneven nucleation hinders the regular generation of the line defects. At sp = 50 μm, wider CF-1s or CF-2s are occasionally generated instead of CF-3s (Figure 4e,g,h; and Figure S9 and Movies S5 and S6, Supporting Information);
7) The translationally invariant configuration textures are observed, having twisted n-field configurations on a cone whose axis is perpendicular to the substrates because they tend to twist at the large d/p. At the beginning of the phase transition, nucleation occurs, similar to the cases of 5) and 6). However, the randomly twisted structures grow around the air pockets upon further cooling (Figure S12b and Movie S8, Supporting Information);
8) No air pockets are generated, and the translationally invariant configuration textures are observed. As described above, the air pockets are generated by the different capillary forces between the patterned and unpatterned areas. However, the capillary forces between the two regions are almost the same when the cell gap is big enough. Eventually, the Ch LC is filled into the intaglio patterns (Figure S12c and Movie S9, Supporting Information).

3. Conclusion

Our experimental results demonstrate that accurate generation and transformation of topological defects can lead to embedding 1D and 2D topological solitons in a uniform far-field with desired spatial locations and geometric configurations. In this sense, our approach can be used as an analogue for the morphogenesis, but here manifested by topological solitons in the Ch LCs and providing insights on the other scales that cannot be readily investigated by experiments.[1–12] In addition, the regularly arranged T3-2s array can open novel avenues for the experimental investigation of spin ice physics.[20,41] The designed reconnection of the disclination lines acting as seed CF-3s can be a laboratory-level experimental platform for gaining insights into behaviors of vortices in superfluids,[42] Bose–Einstein condensates,[43] and cosmology.[44] Finally, the robust and rapid generation of the predesigned solitonic structures in the large area can open up potential applications ranging from memory devices,[19] templates for other materials,[45–47] and all-optical devices.[16,17,25,48]

4. Experimental Section

Sample Preparation and Characterization: 4-Cyano-4″-pentylbiphenyl (5CB, >98%) and dichloromethane were purchased from Sigma-Aldrich. Chiral dopant (S)-4-cyano-4″-(2-methyl butyl) biphenyl (CB15) was purchased from Tokyo Chemical Industry. *N*,*N*-Bis(2,5-di-tert-butylphenyl)-3,4,9,10-perylenedicarboximide (BTBP) was purchased from Sigma-Aldrich. 98 wt% of 5CB was mixed with 2 wt% of CB15 in 1 mL of dichloromethane. The solution was stirred for 1 h at 25 °C and dried under a vacuum. The pitch of the resultant LC was measured with the conventional Grandjean–Cano wedge cell method. Micropatterned silicon wafers with cylindrical patterns were prepared on (100) wafers with photolithography and reactive ion etching. These patterned wafers and pristine glass plates were cleaned using acetone, ethanol, and deionized water. After solvent cleaning procedures, they were treated with O_2 plasma for 5 min to eliminate remaining organic impurities. Both wafer and glass were coated with vertical alignment polyimide (Nissan Chemical) at 3500 rpm for 45 s and were soft-baked at 90 °C for 90 s to evaporate the solvent; they were subsequently cured at 200 °C for 2 h. The substrates were sandwiched with UV curable adhesives and silica microspheres as spacers. The LC mixture was injected slowly into the sandwich cell by capillary action at 40 °C and precisely cooled to 30 °C, which showed the Ch phase with a heating stage (Linkam, LTS420). Optical textures of the Ch LCs were investigated using POM (Nikon, Eclipse LV100POL) with a phase retardation plate (λ = 530 nm) and imaged with a multicolor charge-coupled device camera (Nikon, DS-Ri1). The gaps between sandwich cells were measured using Fabry–Pérot interference with a spectrometer (Ocean Optics, USB-2000+). Fourier transformed images were obtained with ImageJ (freeware from NIH). Fluorescence images of air pockets were obtained with a Fluorescent confocal microscope (FCM) (C2 plus, Nikon) with a laser (λ_{ex} = 488 nm, Coherent). For the FCM imaging, 0.01 wt% of fluorescent dye (BTBP) was mixed with the cholesteric mixture.

Landau–de Gennes Modeling of the Chiral Liquid Crystal: Numerical simulations were used to identify the local configurations and defects of the chiral LCs. The Landau–de Gennes approach describes the free energy of a continuum representation of the LC as

$$F = \iint f_{\text{surface}}\, d^2\mathbf{r} + \iiint f_{\text{bulk}}\, d^3\mathbf{r} \tag{1}$$

where the bulk energy density is integrated over the 3D volume occupied by the LC material, the surface free energies are integrated over the 2D surface from both substrates and air surfaces. The bulk energy density in the Q-tensor representation is

$$\begin{aligned} f_{\text{bulk}} = {} & \frac{A_{\text{LdG}}}{2} Q_{ij} Q_{ji} + \frac{B_{\text{LdG}}}{3} Q_{ij} Q_{jk} Q_{ki} \\ & + \frac{C_{\text{LdG}}}{4} \left(Q_{ij} Q_{ji}\right)^2 + \frac{L_1}{2} \frac{\partial Q_{ij}}{\partial x_k} \frac{\partial Q_{ij}}{\partial x_k} + \frac{L_2}{2} \frac{\partial Q_{ij}}{\partial x_j} \frac{\partial Q_{ik}}{\partial x_k} \\ & + \frac{L_3}{2} \frac{\partial Q_{ij}}{\partial x_k} \frac{\partial Q_{ik}}{\partial x_j} + \frac{L_6}{2} Q_{ij} \frac{\partial Q_{kl}}{\partial x_i} \frac{\partial Q_{kl}}{\partial x_j} + 2 q_0 L_4 \varepsilon_{ikl} Q_{ij} \frac{\partial Q_{lj}}{\partial x_k} \end{aligned} \tag{2}$$

The summation over all indices is assumed, and the molecular tensor order parameter is defined by $Q = \frac{3n \otimes n - I}{2} S$, where $\otimes$ denotes a dyadic product, and S is the scalar order parameter. Here ε_{ikl} is the Levi–Civita symbol and q_0 is the chiral wavenumber parameter related to the pitch, where $q_0 = 2\pi/p$. On the right-hand side of Equation (2), the first three terms are thermotropic parts which describe the nematic-isotropic transition, where A_{LdG}, B_{LdG}, and C_{LdG} are the material parameters. With the minimization of thermotropic energy, the equilibrium scalar order parameter is

$$S_{\text{eq}} = \frac{-B_{\text{LdG}} + \sqrt{B_{\text{LdG}}^2 - 24 A_{\text{LdG}} C_{\text{LdG}}}}{6 C_{\text{LdG}}} \tag{3}$$

The last five terms in Equation (2) are the elastic energy terms that reflect the energy penalty associated with distorting the molecular directors. The orientational elasticity parameters L_i can be related to the Frank–Oseen elastic constants of the LC

$$\begin{aligned} L_1 &= \frac{2}{27 S_{\text{eq}}^2} \left(K_{33} - K_{11} + 3K_{22}\right) \\ L_2 &= \frac{4}{9 S_{\text{eq}}^2} \left(K_{11} - K_{24}\right) \\ L_3 &= \frac{4}{9 S_{\text{eq}}^2} \left(K_{24} - K_{22}\right) \\ L_4 &= \frac{8}{9 S_{\text{eq}}^2} K_{22} \\ L_6 &= \frac{4}{27 S_{\text{eq}}^3} \left(K_{33} - K_{11}\right) \end{aligned} \tag{4}$$

where K_{11}, K_{22}, K_{33}, and K_{24} are the Frank elastic constants describing the energetic costs of splay, twist, bend, and saddle-splay deformations, respectively. For the surface anchoring density, f_{surface} describes the effects of the substrate and air surface on the energy-minimizing local alignment of the LC molecules. Under the perpendicular surface anchoring condition, the surface anchoring density is independent of the azimuthal angle with respect to the surface normal, thus

$$f_{\text{surface}} = \frac{W}{2} \left(Q_{ij} - Q_{ij}^{(0)}\right)^2 \tag{5}$$

where W is the anchoring strength, $Q_{ij}^{(0)}$ is the preferential orientation and order at the surfaces. In simulations, the finite-difference method with the same grid spacing of 10.17 nm in all dimensions was adopted. For the CF-3s structures (Figure S11, Supporting Information), the typical simulation volume is a cuboid box times 120 × 120 × 30, 160 × 160 × 30, 200 × 200 × 30, and 240 × 240 × 30 grid points. By keeping the air pockets diameter (D) equaling 80 points in all cases, D : sp = 1:2, 1:4, 1:6, and 1:8, which correspond to sp = 10, 20, 30, and 40 µm, respectively. For simulating the T3-2 structures, the box sizes are fixed with 100 × 100 × 50 grid points (D = 80 points). To get a stable T3-2 type structure in tensor simulation, the position of one point defect was defined. For all simulations, the following parameters are used, taken

from references.[33–35] $A_{LdG} = -1.72 \times 10^5$ J m^{-3}, $B_{LdG} = -2.12 \times 10^6$ J m^{-3}, $C_{LdG} = 1.73 \times 10^6$ J m^{-3}, $S_{eq} = 0.533$, $K_{11} = 6.4 \times 10^{-11}$ N, $K_{22} = K_{24} = 3 \times 10^{-11}$ N, $K_{33} = 10 \times 10^{-11}$ N, $L_1 = 3.3 \times 10^{-11}$ N, $L_2 = 5.3 \times 10^{-11}$ N, $L_3 = 0$ N, $L_4 = 9.4 \times 10^{-11}$ N, $L_6 = 3.5 \times 10^{-11}$ N, $W_{substrate} = 5 \times 10^{-3}$ J m^{-2} , and $W_{air} = 5 \times 10^{-4}$ J m^{-2}.

Simulation of Polarizing Optical Microscopy Images: The polarizing optical microscopy images were obtained by using the Jones matrix method,[49] where the multiplication of Jones matrices corresponds to the polarizer, analyzer, 530 nm phase retardation plate, silicon wafer, and LC layers with defined patterns of the optical axis orientations. The LC volume was divided into tens of layers, and each layer was treated as a phase retardation plate with spatially varying optical axis and retardation. For the silicon wafer, it was treated as an ideal mirror. To calculate the Jones matrix of each LC grid point, the optical orientation axis direction was defined by the directors, and the ordinary or extraordinary phase retardation was determined by the LC optical anisotropy. To properly approximate the experiment observations, a combination of red, green, and blue color wavelengths (605, 545, and 435 nm) with different intensities was used to match the experiment light source. The light transmission for each wavelength was calculated separately and then superimpose them to get the simulated images (Figures 2j and 3l; and Figures S6 and S11, Supporting Information). The 5CB optical anisotropy $\Delta n = 0.2$ is used in the simulations.

Simulation of Time-Dependent Heat Transfer: The time-dependent heat transfer was calculated by the finite-element method (Figures S2 and S8, Supporting Information). The reported thermal conductivity, density, and heat capacity of 5CB was employed.[50–50] The initial temperature of the sandwich cell filled with 5CB is 37 °C. The top surface of the sandwich cell was cooled by a fixed room temperature of 25 °C. The temperature at the bottom surface of the sandwich cell was cooled from 37 °C with a rate of –0.5 °C min^{-1}.

Statistical Analysis: The data in graphs in Figure 4i,j; and Figure S10 (Supporting Information) were measured with ImageJ (freeware from NIH). All statistical data, including error bars, indicate their mean value extracted from 30 objects. The error bars represent each ± one standard deviation.

Supporting Information

Supporting Information is available from the Wiley Online Library or from the author.

Acknowledgements

G.P., A.S., and H.Z. are contributed equally to this work. This work was supported by the National Research Foundation of Korea (NRF) grant funded by the Korean Government (MSIT) 2017R1E1A1A01072798, 2018R1A5A1025208 (G.P., A.S., C.L., and D.K.Y.), and 2019R1A6A1A10073887 (Y.C.). This research was also partially supported by the U.S. Department of Energy, Office of Basic Energy Sciences, Division of Materials Sciences and Engineering, under Contract No. DE-SC0019293 with the University of Colorado at Boulder (H.Z. and I.I.S.). Computational modeling was supported by the National Science Foundation through Grant Nos. DMR-1810513, ACI-1532235, and ACI-1532236 (RMACC Summit supercomputer).

Conflict of Interest

The authors declare no conflict of interest.

Data Availability Statement

The data that support the findings of this study are available on request from the corresponding author. The data are not publicly available due to privacy or ethical restrictions.

Keywords

chiral liquid crystals, micropatterns, topological defects, topological solitons

Received: February 23, 2022
Revised: May 9, 2022
Published online:

[1] G. S. Adkins, C. R. Nappi, E. Witten, *Nucl. Phys., Sect. B* **1983**, *228*, 552.
[2] T. H. R. Skyrme, *Proc. R. Soc. A* **1961**, *262*, 237.
[3] R. A. Battye, P. M. Sutcliffe, *Phys. Rev. Lett.* **1998**, *81*, 4798.
[4] N. Manton, P. Sutcliffe, *Topological Solitons, Cambridge Monographs on Mathematical Physics*, Cambridge University Press, Cambridge, UK **2004**.
[5] L. Faddeev, A. J. Niemi, *Nature* **1997**, *387*, 58.
[6] A. M. Kosevich, B. A. Ivanov, A. S. Kovalev, *Phys. Rep.* **1990**, *194*, 117.
[7] S. Tsesses, E. Ostrovsky, K. Cohen, B. Gjonaj, N. H. Lindner, G. Bartal, *Science* **2018**, *361*, 993.
[8] S. Takeno, H. Shigeo, *Prog. Theor. Phys.* **1983**, *70*, 308.
[9] F. Büttner, C. Moutafis, M. Schneider, B. Krüger, C. M. Günther, J. Geilhufe, C. V. K. Schmising, J. Mohanty, B. Pfau, S. Schaffert, A. Bisig, M. Foerster, T. Schulz, C. A. F. Vaz, J. H. Franken, H. J. M. Swagten, M. Kläui, S. Eisebitt, *Nat. Phys.* **2015**, *11*, 225.
[10] L. H. Kauffmann, *Knots and Physics*, World Scientific, Singapore **1993**.
[11] C. Adams, *The Knot Book: An Elementary Introduction to the Mathematical Theory of Knots*, American Mathematical Society, Providence, RI, USA **2004**.
[12] G. H. Derrick, *J. Math. Phys.* **1964**, *5*, 1252.
[13] I. I. Smalyukh, Y. Lansac, N. A. Clark, R. P. Trivedi, *Nat. Mater.* **2010**, *9*, 139.
[14] O. Trushkevych, P. Ackerman, W. A. Crossland, I. I. Smalyukh, *Appl. Phys. Lett.* **2010**, *97*, 201906.
[15] P. J. Ackerman, J. Van De Lagemaat, I. I. Smalyukh, *Nat. Commun.* **2015**, *6*, 6012.
[16] A. Varanytsia, G. Posnjak, U. Mur, V. Joshi, K. Darrah, I. Muševič, S. Čopar, L. C. Chien, *Sci. Rep.* **2017**, *7*, 16149.
[17] A. J. Hess, G. Poy, J. S. B. Tai, S. Žumer, I. I. Smalyukh, *Phys. Rev. X* **2020**, *10*, 32.
[18] P. J. Ackerman, I. I. Smalyukh, *Phys. Rev. X* **2017**, *7*, 011006.
[19] J. S. B. Tai, P. J. Ackerman, I. I. Smalyukh, *Proc. Natl. Acad. Sci. USA* **2018**, *115*, 921.
[20] P. J. Ackerman, R. P. Trivedi, B. Senyuk, J. Van De Lagemaat, I. I. Smalyukh, *Phys. Rev. E* **2014**, *90*, 012505.
[21] J. S. B. Tai, I. I. Smalyukh, *Phys. Rev. E* **2020**, *101*, 042702.
[22] I. I. Smalyukh, D. S. Kaputa, A. V. Kachynski, A. N. Kuzmin, P. N. Prasad, *Opt. Express* **2007**, *15*, 4359.
[23] G. Durey, H. R. O. Sohn, P. J. Ackerman, E. Brasselet, I. I. Smalyukh, T. Lopez-Leon, *Soft Matter* **2020**, *16*, 2669.
[24] P. Oswald, J. Baudry, S. Pirkl, *Phys. Rep.* **2000**, *337*, 67.
[25] P. J. Ackerman, Z. Qi, Y. Lin, C. W. Twombly, M. J. Laviada, Y. Lansac, I. I. Smalyukh, *Sci. Rep.* **2012**, *2*, 414.
[26] Y. Guo, S. Afghah, J. Xiang, O. D. Lavrentovich, R. L. B. Selinger, Q. H. Wei, *Soft Matter* **2016**, *12*, 6312.
[27] D. Foster, C. Kind, P. J. Ackerman, J. S. B. Tai, M. R. Dennis, I. I. Smalyukh, *Nat. Phys.* **2019**, *15*, 655.
[28] A. Duzgun, C. Nisoli, *Phys. Rev. Lett.* **2021**, *126*, 47801.
[29] J. S. B. Tai, I. I. Smalyukh, *Science* **2019**, *365*, 1449.
[30] M. Kléman, *Rep. Prog. Phys.* **1989**, *52*, 555.

[31] D. S. Kim, S. Čopar, U. Tkalec, D. K. Yoon, *Sci. Adv.* **2018**, *4*, eaau8064.
[32] G. Park, S. Čopar, A. Suh, M. Yang, U. Tkalec, D. K. Yoon, *ACS Cent. Sci.* **2020**, *6*, 1964.
[33] M. Ravnik, S. Žumer, *Liq. Cryst.* **2009**, *36*, 1201.
[34] D. Seč, S. Čopar, S. Žumer, *Nat. Commun.* **2014**, *5*, 3057.
[35] A. Martinez, M. Ravnik, B. Lucero, R. Visvanathan, S. Žumer, I. I. Smalyukh, *Nat. Mater.* **2014**, *13*, 258.
[36] J. H. Lee, Y. E. Choi, J. H. Lee, B. H. Lee, W. Il Song, K. U. Jeong, G. D. Lee, S. H. Lee, *J. Phys. D: Appl. Phys.* **2013**, *46*, 485503.
[37] R. Zhang, S. A. Redford, P. V. Ruijgrok, N. Kumar, A. Mozaffari, S. Zemsky, A. R. Dinner, V. Vitelli, Z. Bryant, M. L. Gardel, J. J. de Pablo, *Nat. Mater.* **2021**, *20*, 875.
[38] Y. Guo, M. Jiang, C. Peng, K. Sun, O. Yaroshchuk, O. Lavrentovich, Q. H. Wei, *Adv. Mater.* **2016**, *28*, 2353.
[39] G. S. Iannacchione, D. Finotello, *Phys. Rev. Lett.* **1992**, *69*, 2094.
[40] I. Muševič, M. Škarabot, U. Tkalec, M. Ravnik, S. Žumer, *Science* **2006**, *313*, 954.
[41] C. Castelnovo, R. Moessner, S. L. Sondhi, *Nature* **2008**, *451*, 42.
[42] J. Koplik, H. Levine, *Phys. Rev. Lett.* **1993**, *71*, 1375.
[43] S. Serafini, L. Galantucci, E. Iseni, T. Bienaimé, R. N. Bisset, C. F. Barenghi, F. Dalfovo, G. Lamporesi, G. Ferrari, *Phys. Rev. X* **2017**, *7*, 021031.
[44] M. J. Bowick, L. Chandar, E. A. Schiff, A. M. Srivastava, *Science* **1994**, *263*, 943.
[45] E. Lee, Y. Xia, R. C. Ferrier, H. N. Kim, M. A. Gharbi, K. J. Stebe, R. D. Kamien, R. J. Composto, S. Yang, *Adv. Mater.* **2016**, *28*, 2731.
[46] Z. Mai, Y. Yuan, J. S. B. Tai, B. Senyuk, B. Liu, H. Li, Y. Wang, G. Zhou, I. I. Smalyukh, *Adv. Sci.* **2021**, *8*, 2102854.
[47] X. Wang, D. S. Miller, E. Bukusoglu, J. J. De Pablo, N. L. Abbott, *Nat. Mater.* **2016**, *15*, 106.
[48] R. You, Y. S. Choi, M. J. Shin, M. K. Seo, D. K. Yoon, *Adv. Mater. Technol.* **2019**, *4*, 1900454.
[49] H. Mundoor, J. S. Wu, H. H. Wensink, I. I. Smalyukh, *Nature* **2021**, *590*, 268.
[50] J. Deschamps, J. P. M. Trusler, G. Jackson, *J. Phys. Chem. B* **2008**, *112*, 3918.
[51] A. Lebar, Z. Kutnjak, H. Tanaka, B. Zalar, S. Žumer, *Phys. Rev. E* **2008**, *78*, 031707.
[52] A. Boudenne, S. Khaldi, *J. Appl. Polym. Sci.* **2003**, *89*, 481.